High-resolution large area low vacuum scanning electron microscopy (LV-SEM) imaging for microporosity and diagenesis of carbonate rock systems, and carbonate cemented sandstones

Buckman, Jim; Charalampidou, Elma; Zihms, Stephanie; Lewis, Helen; Couples, Gary; Corbett, Patrick; Jiang, Zeyun

Published: 25/06/2017

Document Version
Peer reviewed version

HIGH-RESOLUTION LARGE AREA SCANNING ELECTRON MICROSCOPY: AN IMAGING TOOL FOR POROSITY AND DIAGENESIS OF CARBONATE ROCK SYSTEMS

JIM BUCKMAN, ELMA CHARALAMPIDOU, STEPHANIE ZIHMS, HELEN LEWIS, PATRICK CORBETT, GARY COUPLES, ZEYUN JIANG, AND TIANSHEN HUANG
Institute of Petroleum Engineering, Heriot-Watt University, Riccarton, Edinburgh, EH14 4AS, Scotland
e-mail: j.buckman@hw.ac.uk

ABSTRACT: Automated scanning electron microscopy image collection from geological polished thin sections, in conjunction with autonomous stitching, can be used to construct high-resolution (micron- to submicron-resolution) image montages over areas up to several square centimeters. The technique is here applied to an oolitic limestone and a carbonate laminite to illustrate its application as a tool to study carbonate porosity and diagenesis. Montages constructed from backscattered images are ideally suited to the extraction of data on microporosity, with possibilities including the construction of contoured maps to illustrate the spatial variation in porosity; the construction of porosity logs to illustrate trends in porosity across thin sections; and stochastic construction of digital rock models, for subsequent permeability calculation. Montages taken with a gaseous secondary electron detector in low-vacuum mode can utilize charge contrast imaging (CCI) at a variety of scales and were used here in examining the evolution of carbonate cementation. One example is oolitic limestone, illustrating the formation of grain-lining and pore-occluding cements, as well as recrystallization of the depositional fabric. CCI montages commonly suffer from a variety of contrast and brightness artifacts due to variation in charge distribution across the individual scanned image tiles. Several remedies are discussed that can reduce these artifacts, making it easier to apply image analysis techniques across such montages.

KEY WORDS: porosity, permeability, carbonates, mapping, digital rock models

INTRODUCTION

The term porosity is typically used to encompass not just the scalar percentage of void space per unit volume, but also the size, shape, and distribution, and sometimes connectivity, of these voids. Porosity, or more correctly, the character of the spaces, within carbonates is typically regarded as highly complex and heterogeneous (Hollis et al. 2010, Ott et al. 2015, Pak et al. 2016). It can be divided into a range of sizes (micro-, through meso- to macro- and megascale), although no general consensus exists as to the exact dimensions of the various size classes. The pore size and pore throat size, as well as grain or crystal size, have at some point all been used in pore size classification schemes (Archie 1952; Choquette and Pray 1970; Lucia 1995; Marzouk et al. 1995, 1998; Ramamoorthy et al. 2010; Anovitz and Cole 2015). Nevertheless, various common forms of carbonate pore systems can generally be recognized based on their relationships to the fabric and mode of origin (Choquette and Pray 1970): These have variable shapes, distributions, and degrees of connectivity, and they are either original depositional features, or they are secondary, resulting from diagenetic processes such as dissolution (Fig. 1). In addition, the formation of cements can heavily modify porosity and greatly reduce permeability. Porosity is often much more complex within carbonates, as compared with that found with siliciclastic rocks such as sandstones and mudrocks. The ability to recognize and characterize porosity and its associated pore characteristics, at a range of scales, and to understand changes brought about through diagenesis within carbonate rock systems, is of great significance for understanding these materials' performances as fluid migration pathways, and their role in unconventional hydrocarbon reservoirs and potential for CO_2 storage.

Techniques that can be used to gather geometric/distributional information on such parameters from the micron to the centimeter scale are therefore highly desirable. Optical microscopy has been successfully used in diagenetic studies of carbonates, allowing detailed examination of depositional and authigenic history over the centimeter to sub-millimeter scale, and it is routinely used in porosity studies sensu largo (see Esrafili-Dizaji and Rahimpour-Bonab 2009, Mazurkiewicz and Mlynarczuk 2013, Berrezueta et al. 2015). However, under most normal circumstances, optical microscopy is limited in the size of the pores to which it can be applied, both at the large and the small ends of the scale. Scanning electron microscopy (SEM), however, can image a wider range of pore types, from nano- to macropores, with various architectures.

Other techniques, such as mercury injection capillary pressure and nuclear magnetic resonance, can provide higher-resolution information on porosity (Prammer et al. 1996, Anovitz and Cole 2015, Rios et al. 2015) but do not provide additional information such as pore shape, spatial distribution of pores, or diagenetic alteration of pore networks. X-ray tomography (XRT) provides access to three-dimensional visual data on porosity and pore connectivity (Lebedev et al. 2017), but compared to SEM, it is limited in resolution, and in carbonates, it offers little information on the proportion or type of cement due to the lack of density contrast between cement and matrix. Although SEM is limited to two-dimensional analysis, its ability to image and to differentiate between matrix and cement, or cements, as well as imaging porosity sensu largo over a wide range of scales, makes it one of the most flexible ways to access information on pore space and pore character changes brought about through diagenesis.

Recent developments in electron microscopy allow for the automated imaging and stitching of images to form montages that cover large areas (many centimeters), providing details of the rock fabric at the micron to submicron level (Lemmens and Richards 2013; Buckman 2014; Buckman et al. 2016, 2017). Such montages, together with the individual images (tiles) that comprise them, are ideal for investigating pore space character and distribution using backscattered (BSE) images. In addition, gaseous secondary electron (GSE) images

Carbonate Pore Systems: New Developments and Case Studies
DOI: 10.2110/sepmsp.112.01
SEPM Special Publication No. 112, Copyright © 2018
SEPM (Society for Sedimentary Geology), ISBN 978-1-56576-364-7, eISBN 978-1-56576-365-4, p. 000–000.

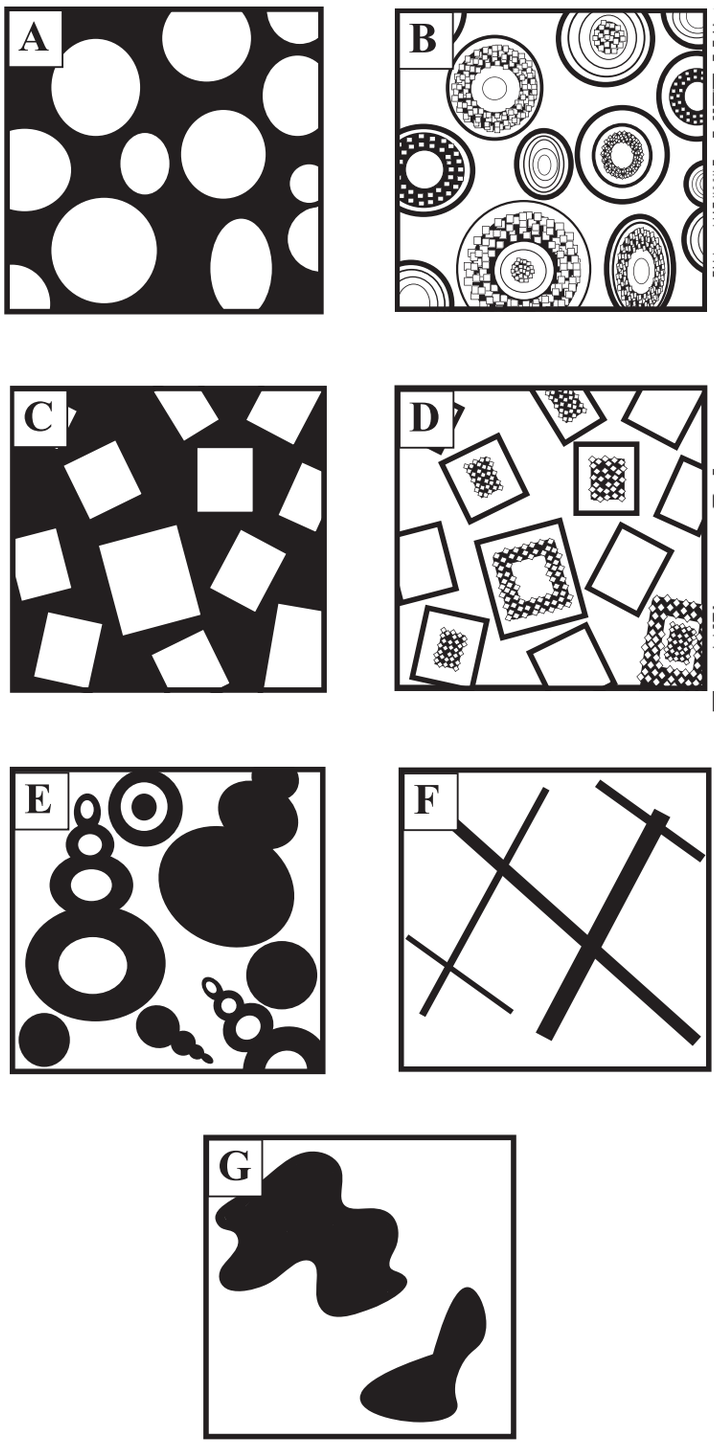

FIG. 1.—Examples of the more common types of porosity associated with carbonates, after Choquette and Pray (1970). **A)** Interparticle, **B)** intraparticle, **C)** intercrystalline, **D)** intracrystalline, **E)** moldic, **F)** fracture, and **G)** vuggy. Porosity is shown in black. Note that porosity illustrated within ooids in (B) was generated by micrite recrystallization, while that in ooids and shelly material in (E) is due to dissolution.

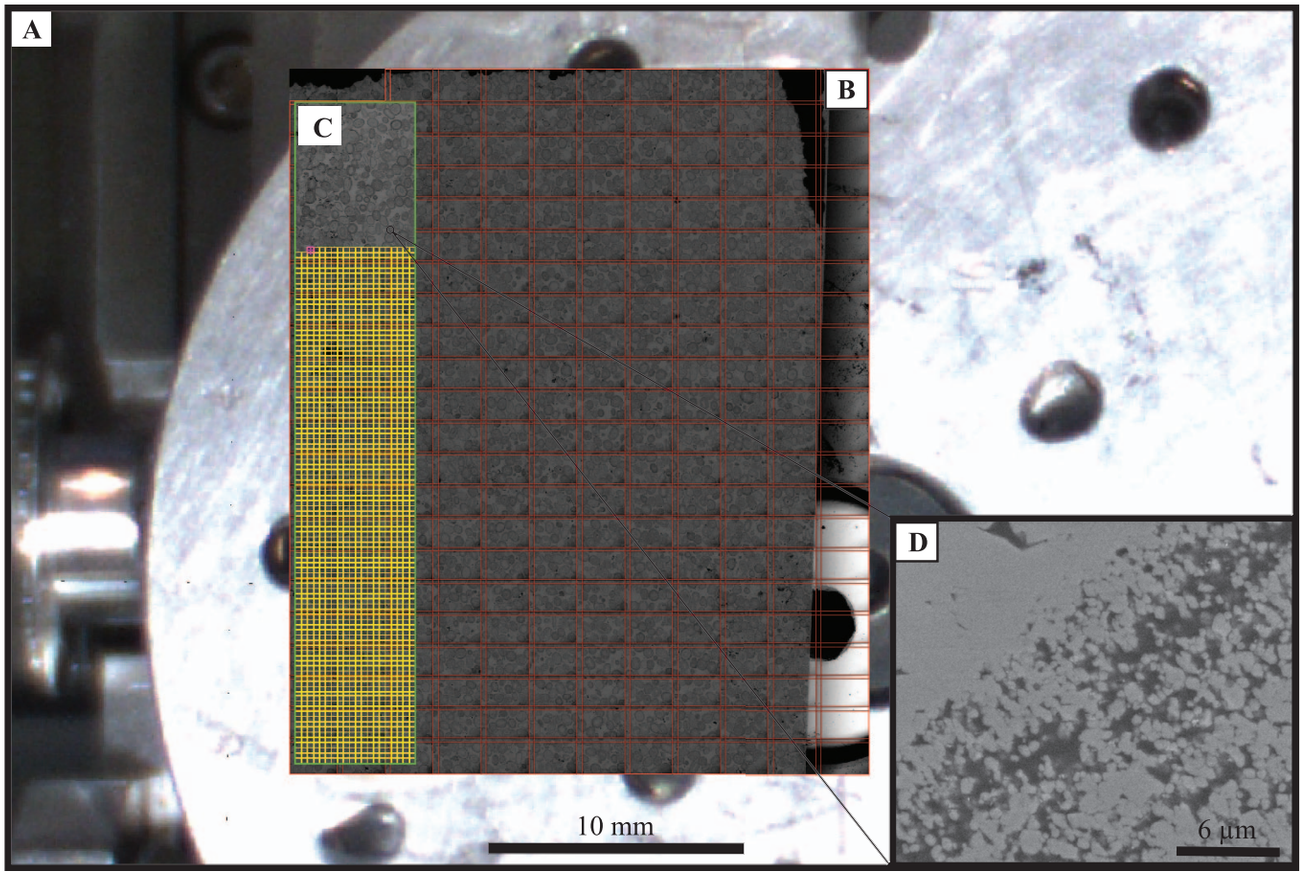

FIG. 2.—Image acquisition using Maps software. **A)** Screenshot showing digital optical overview image acquired through SEM navigation camera. **B)** Low-resolution BSE image of entire polished thin section. Note the discord between BSE image and navigation camera image, illustrating the need for the overview BSE image for accurate location of detailed scans. **C)** Partially collected high-resolution BSE scan from selected area. **D)** Example of single BSE image tile with horizontal field of view of 23 µm.

using the charge contrast imaging (CCI) technique can provide information on cementation and dissolution.

CCI has previously been utilized for imaging geological materials, including carbonates (Watt et al. 2000, Doehne and Carson 2001, Cuthbert and Buckman 2005, Buckman et al. 2016). This technique provides similar results to that of cathodoluminescence scanning electron microscopy (CL-SEM), but it benefits from improved resolution and faster acquisition times (Buckman et al. 2016). The origins of variation in grayscale (through CCI) have been discussed by a number of authors (Griffin 1997, 2000; Buckman et al. 2016) and may reflect subtle variations in elemental composition or, in some cases, physical barriers to electrical conductivity such as different orientations in crystal lattice at hiatuses in crystal growth, or in some cases actual physical breaks (fractures). The construction of large-scale, high-resolution montages using CCI can suffer from acquisition artifacts, but careful selection of instrument parameters can greatly mitigate these problems.

The work reported here acquired high-resolution, large area BSE and GSE CCI images from two carbonates of disparate character to illustrate the kinds of information that can be extracted using this methodology.

MATERIALS AND METHODS

The materials examined were an early Bathonian, Middle Jurassic oolite from Bicqueley Quarry, France, on the east edge of the Paris Basin (48°38′02.4″N, 5°55′43.6″E), and a Cretaceous carbonate laminite from the Araripe Basin of Brazil (7°06′58.7″S, 39°41′48.8″W). Samples were prepared as polished thin sections.

A Quanta 650 field emission gun (FEG) SEM was used, operated in low-vacuum mode at 20 kV, with a water vapor atmosphere at 0.83 Torr, a working distance of 10 mm, and a spot size of 4.5. BSE images were taken with a concentric BSE detector, and GSE images used an off-axis large field gaseous secondary electron detector (LF-GSED).

Both BSE and GSE montages were constructed simultaneously as a series of tiles that were automatically collected and stitched together using "Maps" software from FEI. The procedure followed was similar to that described in Buckman et al. (2017), where an overview image was taken, followed by higher-resolution images acquired from selected areas (Fig. 2). Montages were constructed with a pixel resolution of 1536 by 1024 or 768 by 512, a dwell rate of 10 µs, a range of tile sizes (23, 46, 86, 259 µm for the oolite, 50 and 518 µm for the laminite), and a tile overlap of 10%. In addition, some individual GSE montages were constructed with a tile overlap of 25% or 50%.

Individual BSE tiles were used to analyze porosity and, where relevant, the size, shape, and distributional characteristics of pores in three ways:

1. Two-dimensional (2D) contoured porosity maps were constructed using image analysis of thresholded BSE tiles, following the method of Buckman et al. (2017).
2. Columns of tiles (from method 1) were used to plot 2D vertical porosity values in the manner of borehole porosity logs, producing micron- to millimeter-scale porosity logs.
3. Three-dimensional (3D) stochastic pore networks were constructed, from which permeability was calculated using pore architecture modeling methods (see Wu et al. 2006, Van Dijke et al. 2011, Jiang et al. 2012), using the method of Huang et al. (2018).

Pore network architecture was extracted using in-house software (Huang et al. 2018), utilizing stitched BSE image tiles saved during montage acquisition. The new code allows for improved reconstruction of 3D pore structure through (1) the implementation of an expectation-maximization global optimization algorithm; (2) an adapted k-coherence search algorithm used as an alternative to more commonly used principal component analysis, to reduce loss of pore connectivity; and (3) provision of multithreading to increase computational speed (Huang et al. 2018). In total, 15 porosity network models were constructed for the oolitic limestone; three were constructed from montages stitched together from larger representative areas ($\sim$8 mm^2), and 12 were from smaller areas, each representing approximately one quarter of the area of each of the larger images. Four additional network models were also constructed from cropped individual tiles ($\sim$18 μm^2), each occurring wholly within ooids: Two were from high-porosity areas, and two were from lower-porosity laminae. For the laminite, a representative montage with an area of 3 mm^2 was acquired that illustrated the variability in laminae type, with four additional images cropped from individual tiles within high- and low-porosity regions, with areas of 32.5 μm^2. BSE images were binarized using ImageJ and then cropped to a square format (vertical height equal to horizontal field of view) and rescaled to produce 400 by 400 pixel training images (Figs. 3, 4), with a corresponding reduction in pixel resolution (Table 1). Most porosity networks were constructed using a single training image for the X, Y, and Z planes. However, for "Laminite1," the representative training image (X) was modified by rotating the image through 45° and 90°, to produce individual images for the X, Y, and Z planes, which was necessary to construct a realistic layered model for this strongly heterogeneous laminated material. All models were stochastically constructed to produce pore architecture models that matched porosity as well as pore shape and the training image pattern. The models produced were all 400 by 400 by 400 voxels in dimension, to help facilitate faster processing during pore network reconstruction.

Reconstructed 3D pore structure models were then further processed using in-house pore analysis tool (PAT) software (Wu et al. 2006), which fits a pore network model that was used to calculate permeability. In pore network models, pore bodies are represented as spherical nodes, and pore throats are represented as connecting bonds (Wu et al. 2006, Jiang et al. 2007, Ryazanov et al. 2009). Compared to the often used lattice-Boltzmann method (cf. Chen et al. 2015, Hosa et al. 2016), this saves on computational effort, which can be of particular importance for large, highly complex rock pore systems. Additionally, in the case of the laminite model, Heriot-Watt 2phase Pore Network Modelling software was used to determine the distribution of connected versus disconnected pores.

Although BSE images and montages can be readily used to extract details on porosity, they provide limited information on the nature of cement. Therefore, GSE images and montages utilizing the CCI technique were also collected, which provided plentiful information on cement development and therefore on changes in porosity during geological time. CCI utilizing the LF-GSED was used to demonstrate how the diagenetic history of the samples could be investigated through the examination of cements in order to illustrate changes in porosity over time (see method in Buckman et al. 2016).

RESULTS

BSE Montages

BSE images and montages of polished thin sections clearly indicate the occurrence of pores within both the oolitic limestone and laminite, which are represented at the darker end of the grayscale (Figs. 2D, 5A). These images can be used to quantitatively extract data on porosity, as well as for 3D modelling of porosity and permeability.

Contoured Porosity Percentage Maps: High-resolution contoured porosity percentage maps for the oolitic limestone, based on montaged BSE images (Fig. 5A), display a clear picture of the distribution of porosity within the limestone (Fig. 5B–D). The contoured maps graphically confirm observations from the BSE montage showing that porosity is typically low and confined to the particulate component (intraparticle porosity within ooids), which is the opposite to what would originally have been found upon deposition of the limestone. Porosity within ooids is observed to occur as a series of concentric bands, although not all ooids display high porosity (Fig. 5). The distribution of pore density is highly sporadic (Fig. 5B–E).

Porosity maps for the laminite (Fig. 6B–E) clearly illustrate that porosity occurs in bedding-parallel laminae (confirming the findings of Buckman et al. 2017). Most of the laminite is composed of areas of relatively low porosity (less than 5%), with higher-porosity laminae (up to 12%) restricted to the upper part of the sample (Fig. 6B). Porosity between laminae is highly variable, and this is particularly evident from the exploded section (Fig. 6E), showing multiple thin higher-porosity laminae with maximum porosity of 70%. It is noteworthy that the latter are not necessarily spatially persistent, and they are highly heterogeneous.

Microlog Linear Porosity Trend: Measured porosity values were plotted as linear changes in porosity through the samples and illustrated in the manner of a borehole geophysical "log" (Figs. 6C, 6F, 7B). Comparison of the three vertical micrologs illustrated for the oolite shows that porosity does not occur in a predictable microstratigraphic fashion (Fig. 7), but it confirms that high-porosity regions are more randomly distributed, occurring within individual ooids (intraparticle microporosity). Average porosity values display a more consistent 10 to 20%. In contrast, porosity micrologs for the laminite display major changes across laminae, with individual logs showing good agreement with each other (Fig. 6F); therefore, average porosity values (Fig. 6C) through the whole thin section are adequate for recording vertical porosity trends.

Stochastic Modeling: Models constructed from the larger area oolite training images (Oolite1–3) record porosities of 13 to 20% and permeabilities (horizontal and vertical) of 164 to 472 mD, whereas the smaller (medium-sized) subsets (Oolite1a, 1b, 1c…3d) recorded porosities of 14 to 24% and permeabilities of 34 to 191 mD, with the majority below 150 mD (Table 2). A representative selection of models constructed for the oolitic limestone is illustrated in Figure 8. Models reconstructed from within individual ooids (OoidA, B, C, D) correspond to intraparticle microporosity and record porosities of approximately 50 to 70%, with corresponding average permeability of 2 to 6 mD, and 16% porosity with approximately 0.06 mD permeability, respectively (Table 2). For the larger representative area modeled for the laminite (Laminite1), porosity of 7% and permeability

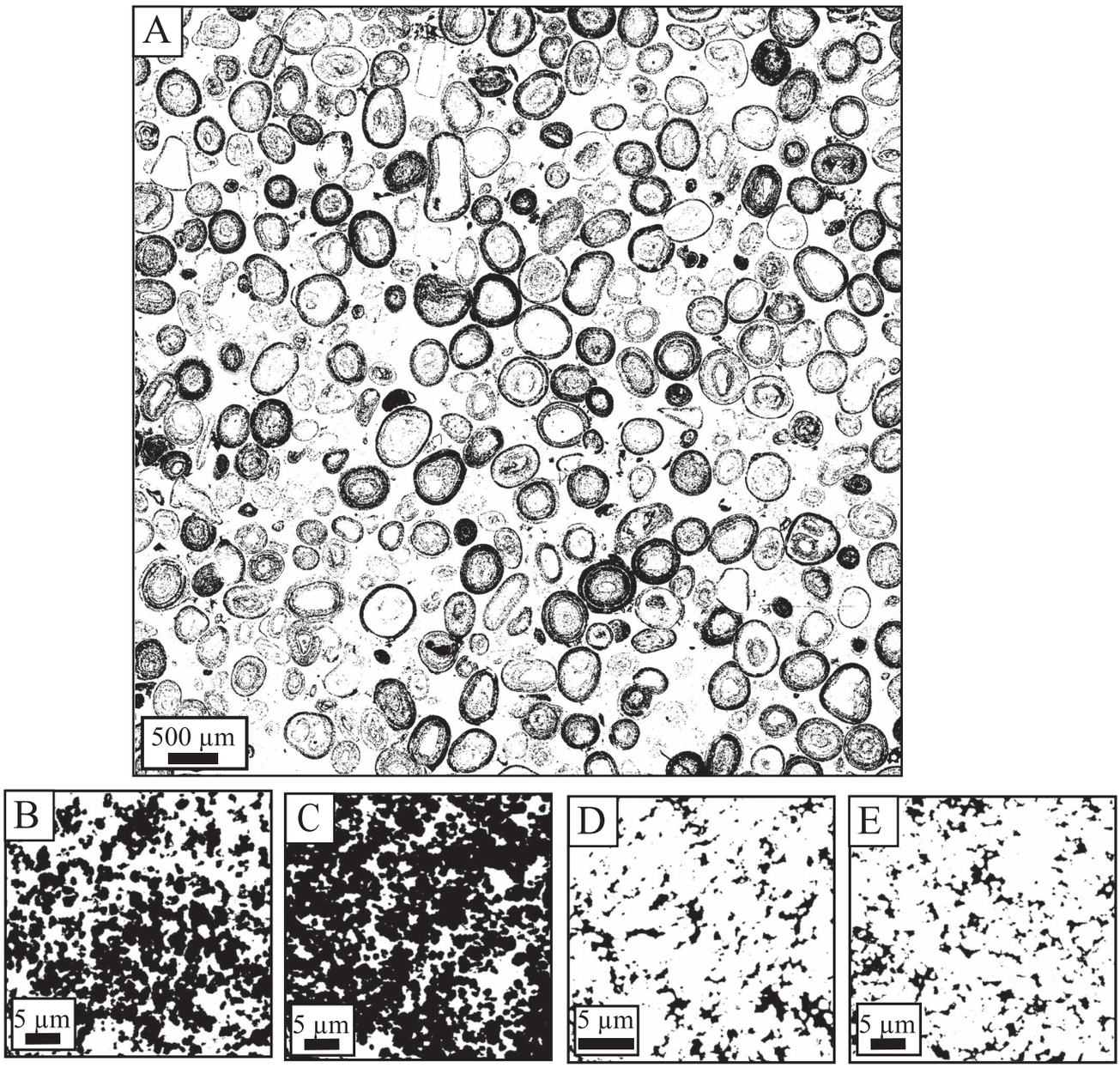

FIG. 3.—Illustrations of examples of training images used in stochastic reconstruction models. **A)** Whole-rock training image for Oolite1. **B)–E)** OoidA to OoidD, representing higher resolution of individual ooids. All training images were 400 by 400 pixels. For pixel resolution, see Table 1.

values of less than 0.01 mD perpendicular to bedding, and 26.10 mD parallel to bedding, respectively, were modeled. Individual high-porosity lamellae (LaminiteA, B) gave porosity of 19 to 26% and permeability of 1.37 to 3.00 mD, and lower-porosity regions gave approximately 3 to 4% porosity with negligible permeability (Fig. 9; Table 3). In addition, flow modeling of the large laminite model visually demonstrates the lack of connectivity across laminae (Fig. 9B) and a high degree of pore connection parallel to the more porous laminae, although even in this case, not all pores are necessarily connected (Fig. 9C).

GSE-CCI Montages

CCI montages of the oolite display a range of diagenetic features, notably several generations of isopachous rimming cements around individual ooids (Fig. 10), a coarser pore-filling equant cement phase (Fig. 10B–E), and recrystallized matrix within ooids (Fig. 11).

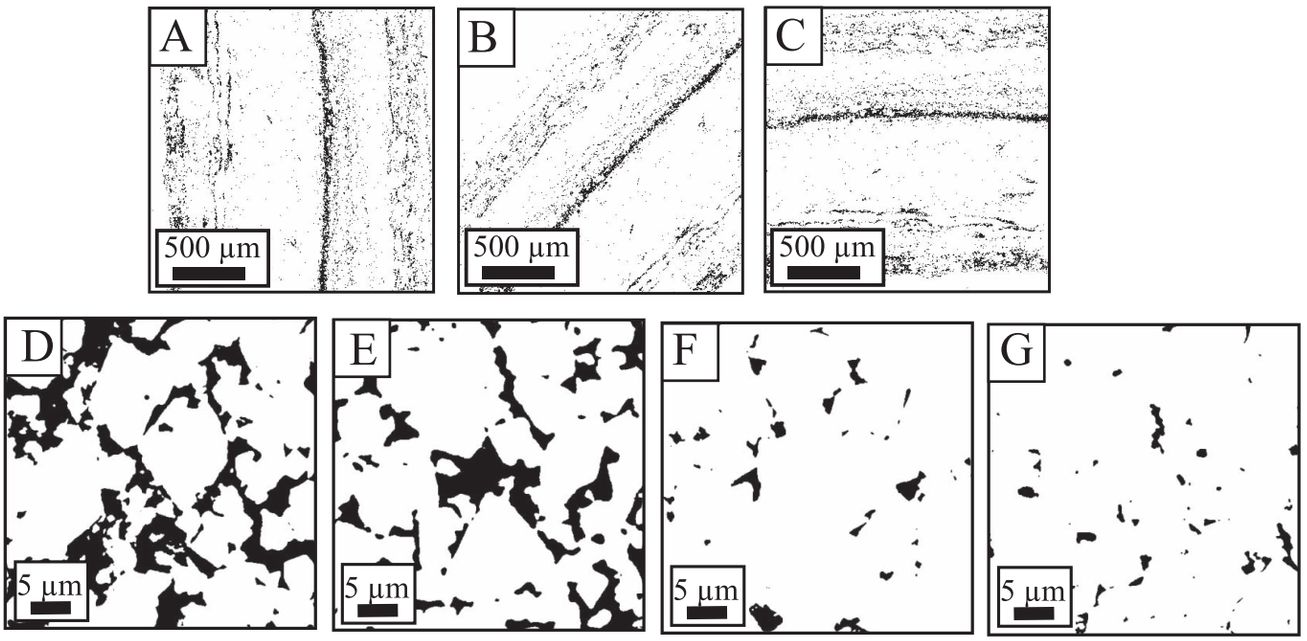

FIG. 4.—Illustrations of examples of training images used in stochastic reconstruction models. **A)–C)** Whole-rock training images for Laminite1. **D)–G)** LaminiteA to LaminiteD, representing higher resolution of individual laminae. All training images were 400 by 400 pixels. For pixel resolution, see Table 1.

Isopachous cement typically occurs in two distinct phases. An initial rimming cement of fine crystals (~10-μm-thick zone) that are radially developed, and typically appear brighter in CCI images (Fig. 10A, B, D–F), is followed by a coarser (up to 50 μm thick), often more equant isopachous cement. The latter can either form rims that are continuously developed about the ooids, or it occurs as more isolated "tooth-like" developments (Fig. 10E). The appearance of the coarser isopachous cement crystals is more variable in nature, with CCI delineating a series of growth phases (observed as differing gray levels), which are often accompanied by a change in crystal shape (Fig. 10C). Additionally, CCI can also highlight micron- to submicron-scale growth increments (Fig. 10G, H). Well-developed crystal faces indicate growth into unobstructed fluid-filled pore space (Fig. 10E).

Pore-filling cements occur in a variety of sizes, but they are typically much coarser (up to 100 μm) than is the isopachous cement (Fig. 10B). Pore-filling cements are typically equant, but they generally lack any internal structure in CCI, although they occasionally display broad growth increments (Fig. 10B).

Close examination of the matrix of ooids indicates a series of floating equant (rhombic) micron-sized crystals (Fig. 11C–F) that replace the original ooid fabric. In rare cases, the "ghosts" of original micritic fabric were observed (Fig. 11A, B).

Compared to the oolite sample, GSE images of the laminite were less informative. However, the CCI technique did illuminate details of rhombic crystals, for which no information was available through the analysis of BSE images (Fig. 12A, B). The occurrence of such rhombic crystals is suggested (BSE images) by the observation of diamond-shaped pits (Fig. 12A), although the majority of crystals were only observed in the CCI image (Fig. 12C, D). The matrix surrounding the rhombic calcite crystals appears to be coarse sparry calcite, indicating recrystallization of much of the original matrix material.

TABLE 1.—Original SEM image horizontal field of view (HFOV) pixel width and pixel resolution versus training image pixel width and pixel resolution (res).

		Original SEM image		Training image	
Sample	HFOV (μm)	Pixel width	Pixel res	Pixel width	Pixel res
Oolite1, 2, 3	~7600	24,000	271 nm	400	18.5 μm
Oolite1a, 1b, etc.	~3800	14,000	271 nm	400	9.5 μm
OoidA, B, etc.	~17.6	800	22 nm	400	44 nm
Laminite1	~2850	8640	337 nm	400	7.12 μm
LaminiteA, B, etc.	~32.5	500	65 nm	400	81 nm

DISCUSSION

The combination of BSE and GSE-CCI image montages can be utilized to clearly demonstrate porosity (BSE images), as well as gather information about the ways in which pores have changed through time with cementation (CCI images).

BSE Montages and Tiles

Contoured Porosity Maps and Linear Porosity Logs: The use of BSE tiled images collected and processed to form contoured porosity maps has previously been outlined as a technique for visualizing porosity variation within carbonates (Buckman et al. 2017). The current work confirms the usefulness of this technique in relationship to other carbonates. In the case of the oolite, the use of the technique

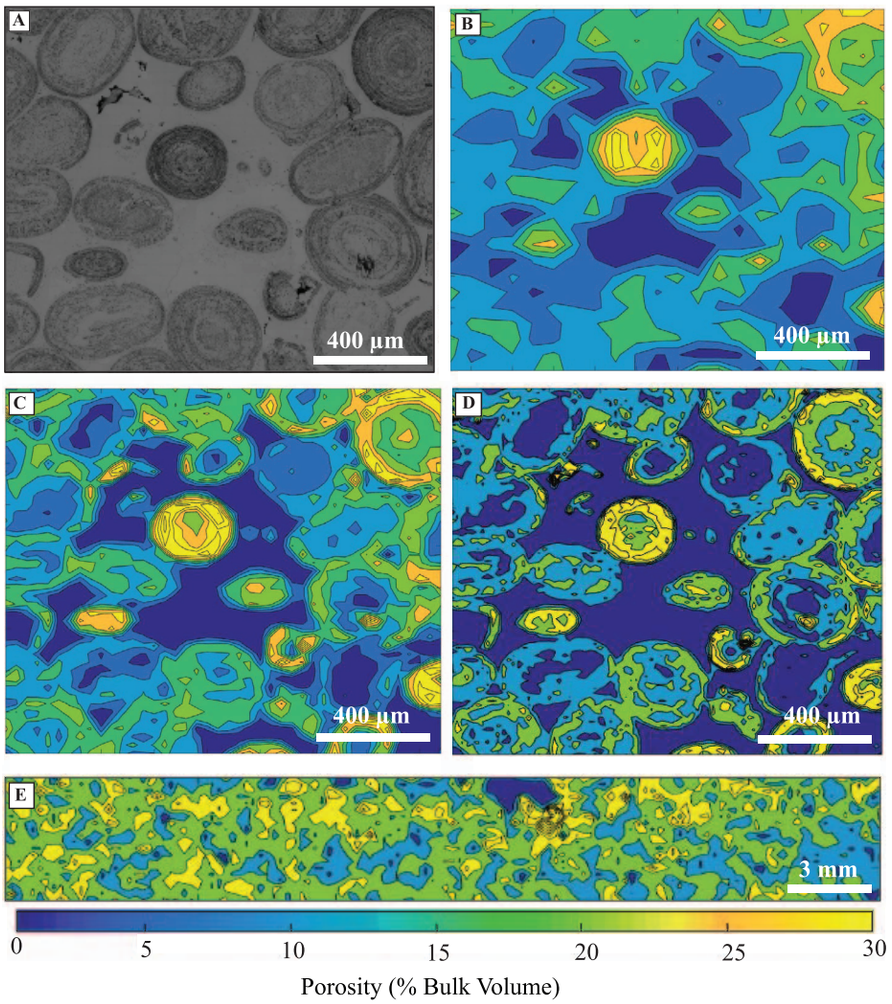

FIG. 5.—Illustration of BSE tiled montage and associated color-contoured maps for percentage porosity for the same area at various tile sizes/resolutions for the oolitic limestone sample. **A)** BSE montage of a selected area of the oolite, approximately 1.5 mm in width, individual tile size as in (C). **B)** Color-contoured map of percentage porosity based on area in (A) with 22 by 24 tiles, each with a horizontal width of 86 µm. **C)** As in (B) but 46 µm tiles (42 by 45). **D)** As in (B) and (C) but 23 µm tiles (85 by 90). Illustrating increased resolution in porosity maps from (B) to (C). Note increasing resolution requires longer image acquisition from 1 hour to 3 and 12 hours, respectively. **E)** Contoured porosity montage (approximately 30 by 5 mm in area) of a different area at lower resolution (259 µm tiles), illustrating variability in porosity across a larger area.

can accurately portray variation in porosity, illustrating the restriction of high porosity to particular ooids, or certain laminae within ooids (Fig. 5). As with previous work, although general trends in porosity change are clearly observed with larger-sized tiles, it is apparent that higher-resolution tiles are required to extract the finer details of porosity variation therein (Fig. 5D). In this case, the spatial variation in porosity clearly indicates that the highest values of porosity are typically restricted to ooids (intraparticle microporosity), with pores previously present between ooids (interparticle porosity) becoming heavily cemented with minimal porosity preserved. In this example, the additional time required to acquire the higher-resolution data may be of limited practical use, as these intraparticle pores are unlikely to be interconnected, and thus permeability will be low. The exception to this would occur in relationship to fracking, where the development of new fracture systems would considerably open up permeability, as would acidification, through connection of otherwise isolated intraparticle microporosity. This may prove significant in CO_2 storage applications. Where a high level of detail is not required, larger tile sizes can be used over more extensive areas (Fig. 5E) to extrapolate general trends in porosity across areas that could be several square centimeters in size, and these larger tile sizes would require much less time to collect. The laminite larger area porosity contour map (Fig. 6B) confirms the high degree of variability in pores between laminae, as previously illustrated in Buckman et al. (2017), but it also indicates that much of the laminite is composed of areas of very low to negligible porosity. Contoured porosity plots for both carbonates are particularly useful in their graphical illustration of pore distribution in two dimensions.

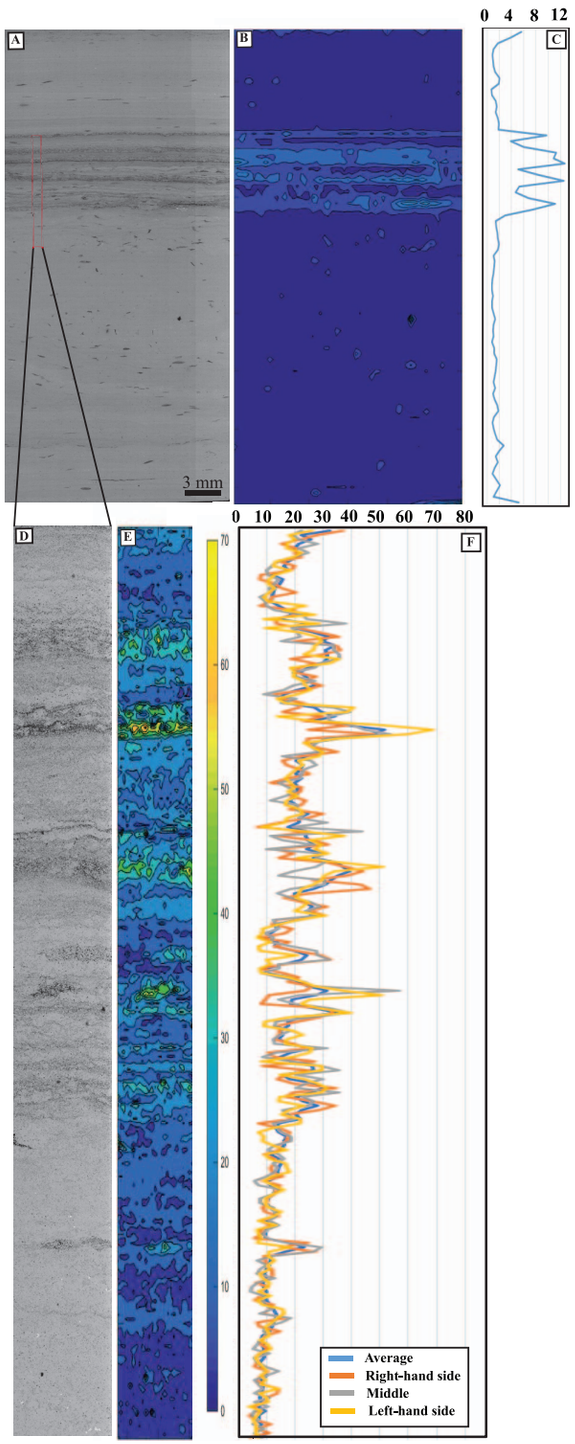

FIG. 6.—Illustration of BSE tiled montage and associated color-contoured maps for percentage porosity for the laminate sample. **A)** BSE tiled montage of whole slide. Red box illustrates area shown in (D) and (E). **B)** Colored contour plot showing relative abundance of porosity from area illustrated in (A). Dark blue = lowest porosity; turquoise to green = higher porosity. **C)** Microporosity log through section. Average porosity trend is illustrated. **D), E)** BSE montage and color-contoured porosity map of area within red box of (A), respectively. Dark blue = lowest porosity; orange and yellow = areas of higher porosity. **F)** Linear porosity plots (porosity increasing to the right) through random vertical positions in (D). Note close correspondence of the three porosity trends and average values. (A), (D), and (E) are based on Buckman et al. (2017).

TABLE 2.—Modeled porosity and permeability data for oolite.

Model No.	Porosity (%)	Average permeability (mD)
Oolite1	20.08	472.37
Oolite1a	23.18	145.50
Oolite1b	24.03	191.40
Oolite1c	20.82	127.84
Oolite1d	24.03	162.09
Oolite2	13.01	164.02
Oolite2a	14.44	76.88
Oolite2b	14.37	34.89
Oolite2c	16.85	87.52
Oolite2d	13.44	48.89
Oolite3	17.52	345.02
Oolite3a	24.01	136.97
Oolite3b	20.55	160.02
Oolite3c	21.90	172.74
Oolite3d	16.99	87.52
OoidA	52.69	2.07
OoidB	72.96	6.36
OoidC	16.72	0.06
OoidD	16.53	0.05

In the case of laminated carbonates, or other carbonates where there are changes in porosity in the vertical direction, simpler linear porosity trends can be more easily and quickly plotted (Fig. 6C, F). Such plots are similar in construction to borehole porosity logs. Logs are, however, less helpful where porosity is more heterogeneous in distribution, such as in the oolite (Fig. 7B).

Stochastic Modeling: The examples of 3D stochastic models for porosity and permeability produced for both limestones illustrate the potential for utilizing BSE SEM images, collected as automated high-resolution large area montages, to model pore networks in three dimensions and to reconstruct indicative information on permeability. In this case, this was undertaken at the "whole rock" and the "lamina" scales. Potential also exists to further extract data on pore geometry, size, pore throat size, tortuosity, connectivity, and responses to imbibition and drainage representative of standard core flooding tests (Wu et al. 2006, Ryazanov et al. 2009, Van Dijke et al. 2011, Jiang et al. 2012).

Representativeness of Porosity Permeability Network Models: There exist major differences in permeability predicted for the oolite for the two sizes of training images (Table 2), with values derived from the larger training images approximately twice those of the equivalent medium-sized subsets. It may be that the larger-scale training images result in an apparent increased pore connectivity when

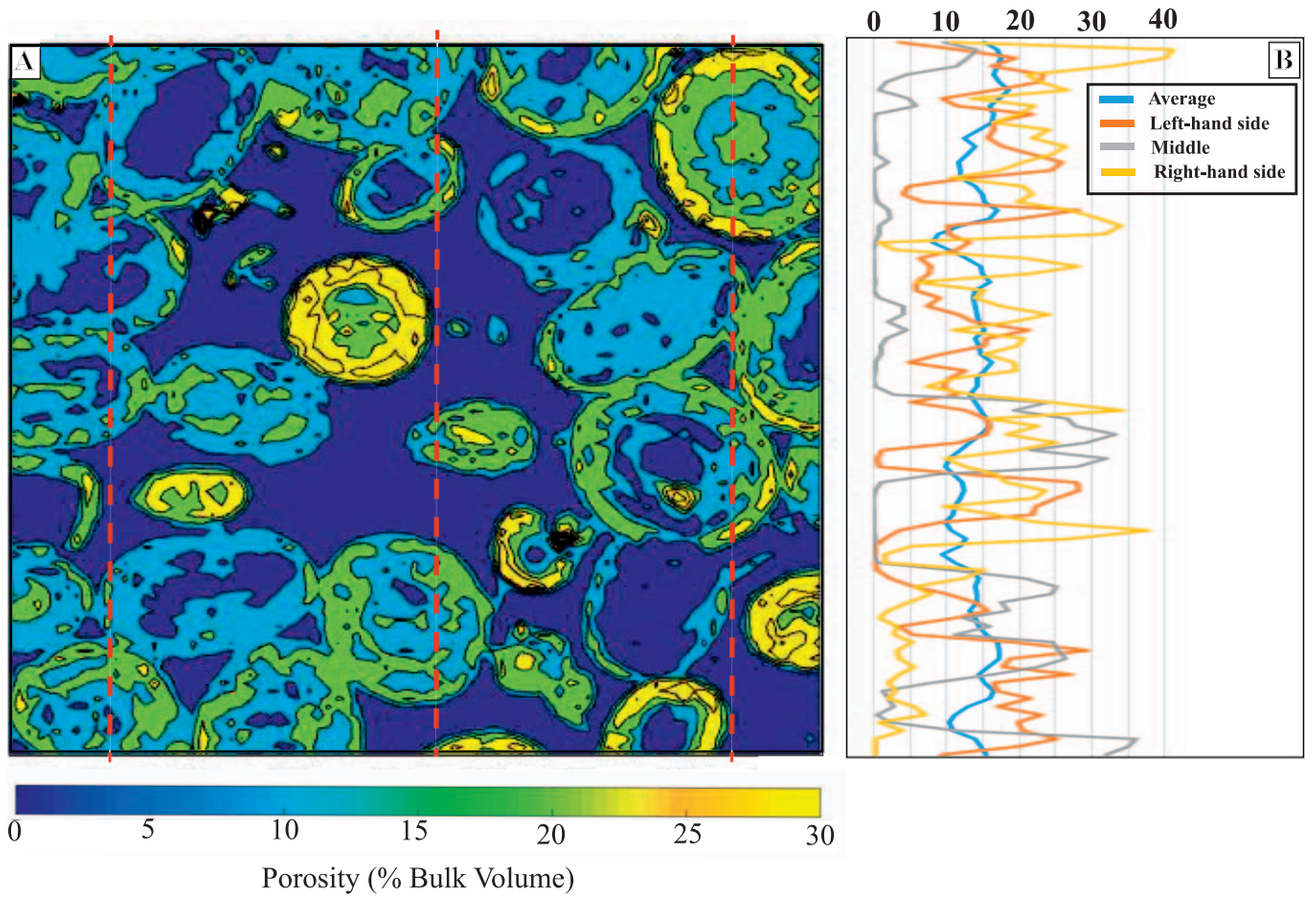

FIG. 7.—Illustration of color-contoured porosity map and corresponding vertical porosity trends for oolitic limestone. **A)** Color-contoured porosity map as in Fig. 5D. **B)** Three random representative vertical porosity trends, through (A), with approximate positions marked by dashed red lines. Note no clear agreement between porosity trend lines, due to variable distribution of ooids, and high variability of intraparticle porosity within individual ooids. Average value shows low variability.

scaled to fit the 400 by 400 by 400 voxel models, resulting in overly high permeabilities.

Zinszner and Pellerin (2007) recorded a broad range in permeability that encompasses the range of predicted values from the current model reconstructions, from 1.50 mD to 2 D for those oolitic limestones with 25% porosity. Their high variability is due to the relative abundance of connected interparticle porosity versus intraparticle microporosity

TABLE 3.—Modeled porosity and permeability data for laminite.

		Permeability (mD)			
Model No.	Porosity (%)	X	Y	Z	Average*
Laminite1	6.96	0.0030	26.0815	0.0005	—
LaminiteA	26.04	2.6122	3.0012	2.4842	2.6992
LaminiteB	19.01	1.4410	1.3671	1.4793	1.4291
LaminiteC	4.15	0.0015	0.0026	0.0022	0.0021
LaminiteD	3.29	0.0001	0.0000	0.0000	0.0000

* No average given for Laminite1, due to strong heterogeneity in permeability.

associated with recrystallization of micritic ooid laminae (or macromoldic porosity, from dissolution of ooids), with the latter playing little part in permeability. The current material has a high degree of isolated intraparticle microporosity (and little or no macromoldic porosity) with a general lack of well-developed or connected interparticle porosity, which should lead to a permeability in the millidarcy range rather than in the darcy range.

Permeability values derived from the larger training image reconstructions fall within the range of values calculated by Moh'd (2009) from vuggy French Jurassic oolitic limestone (Savonnieres limestone) of similar texture and porosity to the current material (Table 4). However, values recorded by Moh'd (2009) were calculated using the "Jorgensen equation" rather than being measured directly. Lebedev et al. (2017), also studying the Savonnieres limestone, used direct gas permeametry to record a permeability in the region of 30 mD, and used X-ray tomography to record a permeability of 6.75 mD using brine injection (Table 4). The former is closer to several of the values predicted by some of the current medium-sized subsets of training images (although less than in the majority), whereas the latter value measured through brine injection is comparable with the permeability value predicted using training image "OoidB" of 6.36 mD (Table 2) for intraparticle microporosity within ooids. Values of

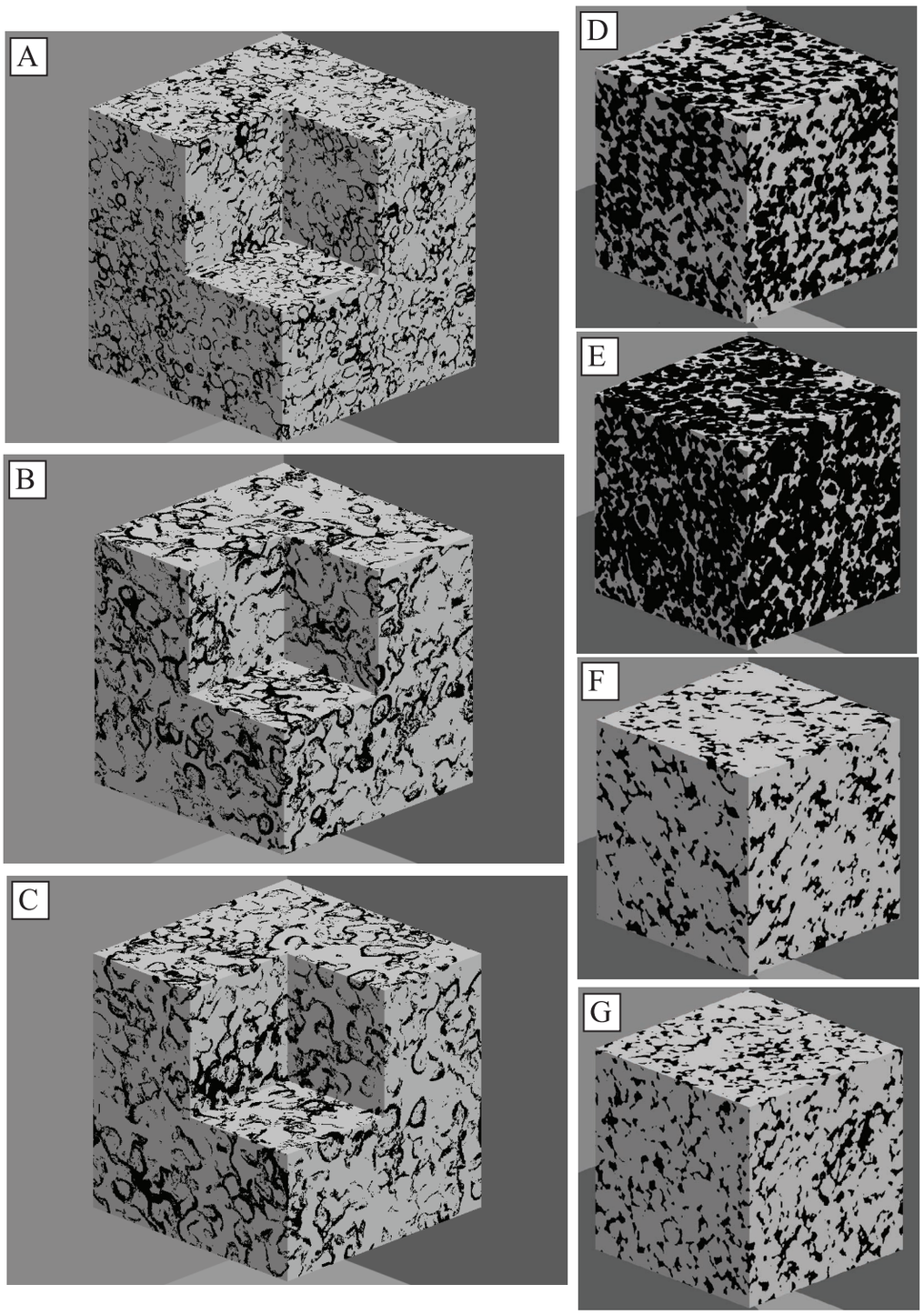

FIG. 8.—Representative three-dimensional porosity network models, generated for oolitic limestone sample. **A)** Oolite1, **B)** Oolite1a, **C)** Oolite1d, **D)–G)** OoidA to OoidD. (A)–(C) Whole-rock reconstructions; (B) and (C) higher-resolution models derived from approximately ¼ of the SEM image used to construct (A); (D)–(G) models constructed from training images representing porosity within individual ooids. All models are 400 by 400 by 400 voxels. Voxel resolution as per pixel resolution of corresponding training image pixel resolution (see Table 1). See Table 2 for corresponding porosity and permeability values.

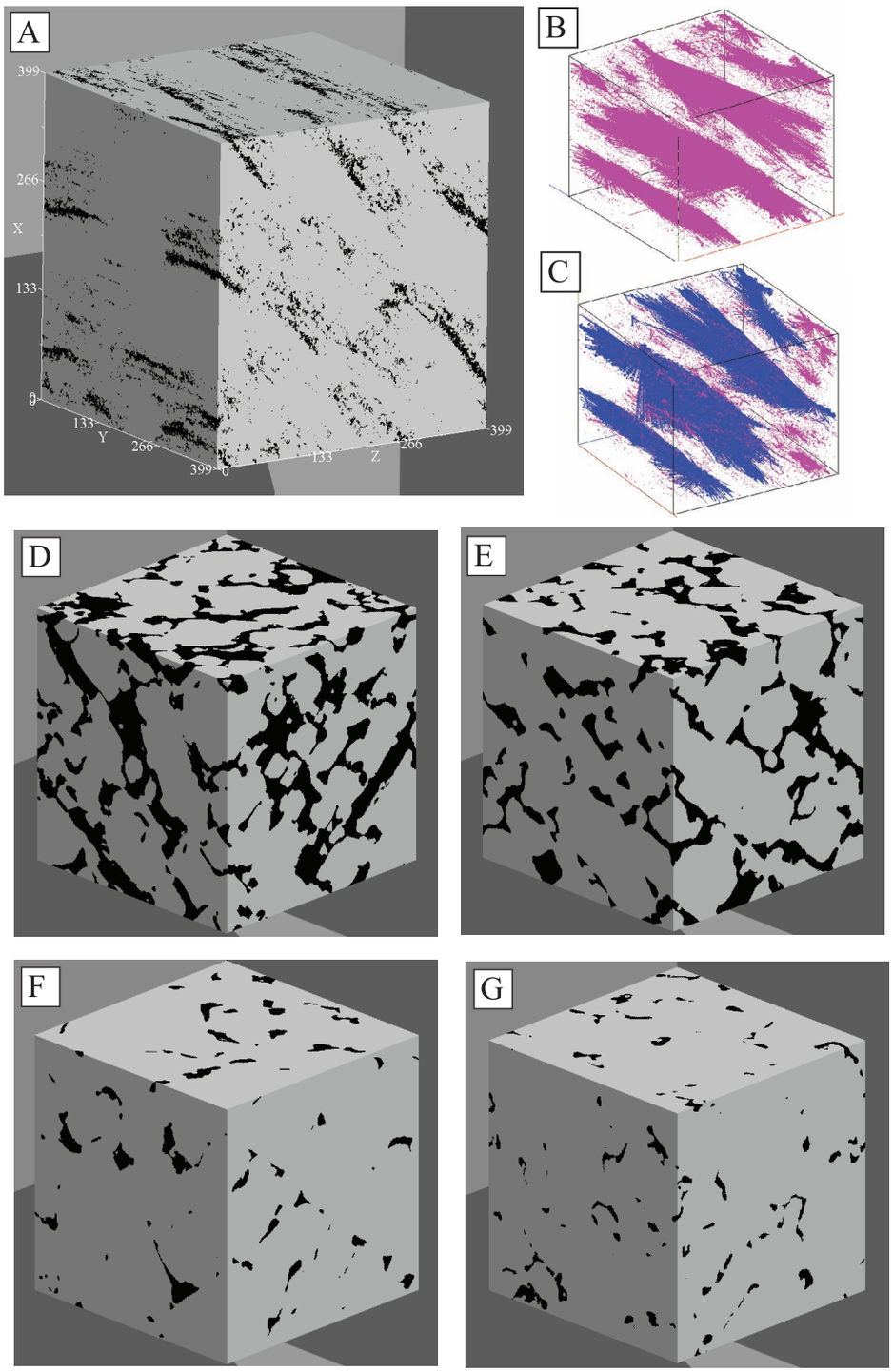

FIG. 9.—Representative three-dimensional porosity network models and flow models generated for laminite sample. **A)** Pore network model for Laminite1, with X, Y, and Z axes marked, and **B)** and **C)** flow models for model in (A), illustrating pore connectivity, with models approximately in the same orientation; (B) flow across laminae (along X or Z axis); (C) flow parallel to laminae (along Y axis), pink = isolated, blue = connected. **D)** and **E)** Models of more porous laminae, and **F)** and **G)** less porous laminae. All models are 400 by 400 by 400 voxels. Voxel resolution as per pixel resolution of corresponding training image pixel resolution (see Table 1). See Table 3 for corresponding porosity and permeability values.

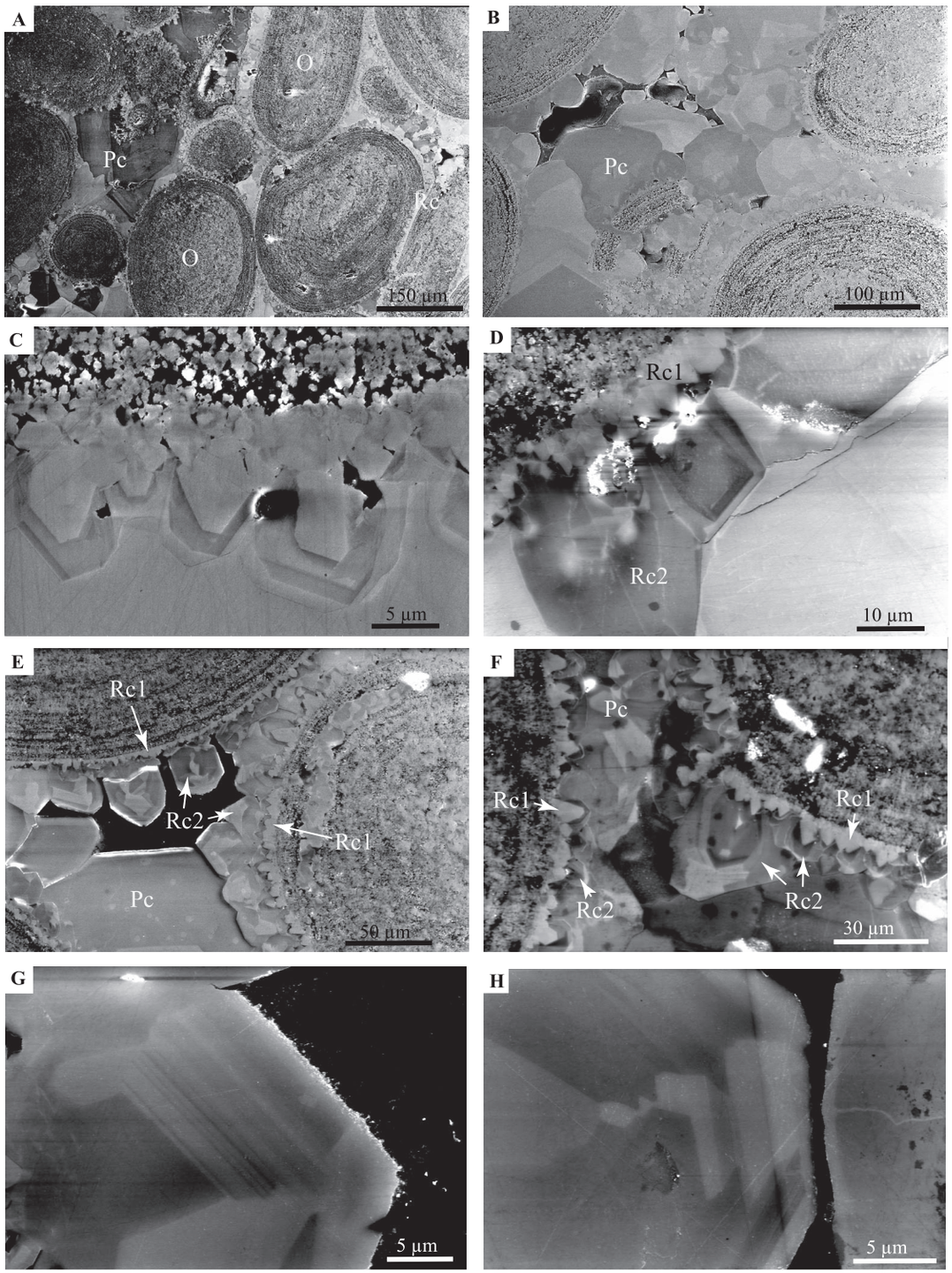

FIG. 10.—CCI of oolitic limestone, using GSE detector, from montaged areas and single tiles. **A)** Montaged image showing whole ooids (O), rimming cement (Rc), and sparry pore-filling cement (Pc). **B)** Coarse sparry calcite infilling porosity between ooids. **C)** to **F)** Details of ooid-rimming cements, exhibiting multiple growth phases and two size ranges (Rc1 and Rc2). Note that in (D)–(F), the initial finer rimming cement is paler and less complex in appearance than the following coarser rimming cement. **G)** and **H)** Details of coarser rimming cement, displaying incremental growth phases, and micron- to submicron-scale growth laminae in (G).

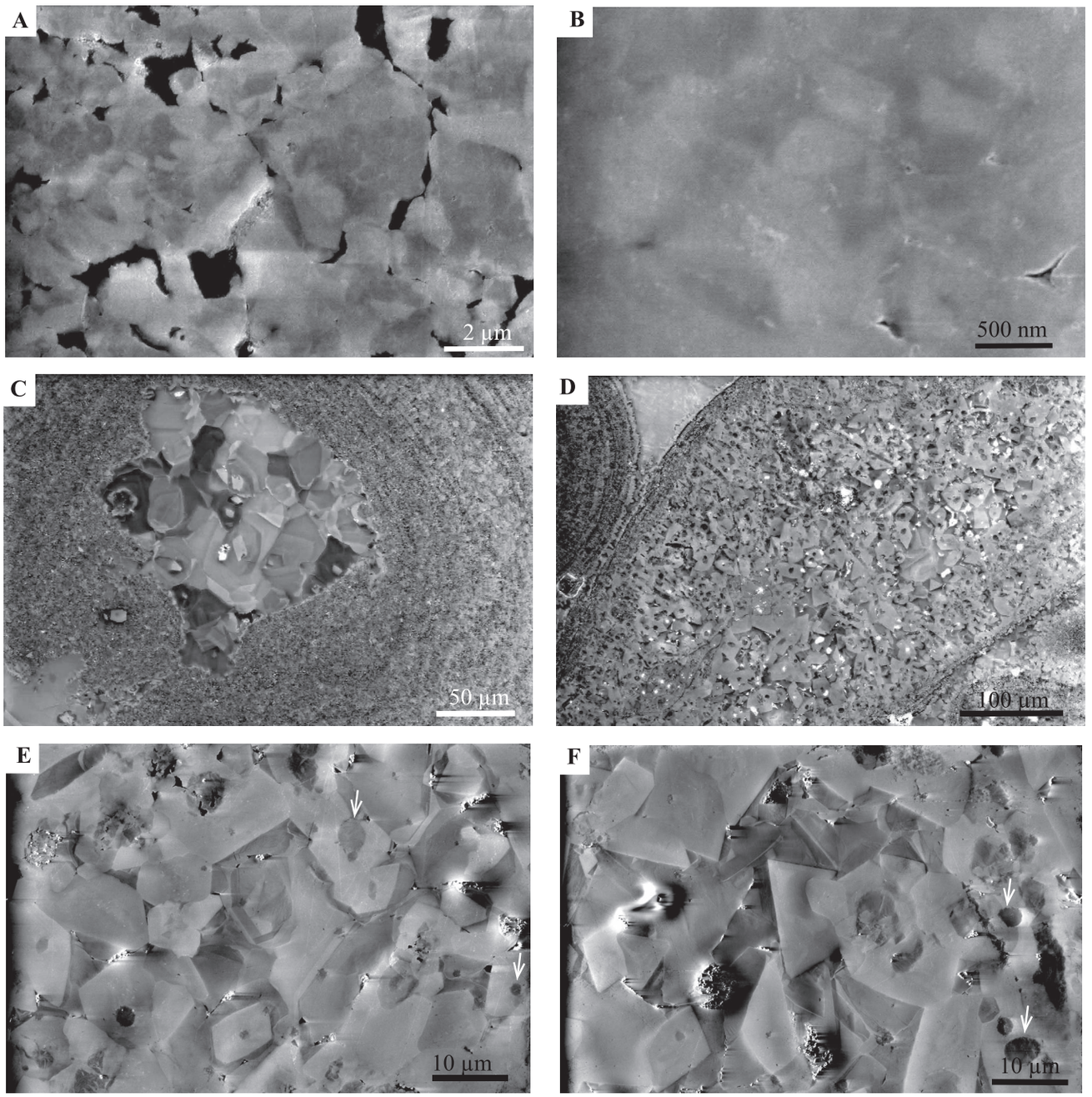

FIG. 11.—CCI of oolitic limestone, using GSE detector. **A)** and **B)** Ghost-like micritic particles at the center of ooids, replaced by later cement. **C)** Patch of sparry cement at the center of an ooid, in (?) dissolution cavity. **D)** Irregularly intergrown crystals replacing original ooid fabric. **E)** and **F)** Details of crystals in (D), showing complex intergrowth of cement, with many centered around darker "spheroidal" cores (arrows).

permeability measured for other oolitic limestones from the Permo–Triassic of the Persian Gulf, with similar porosity values to that of the current material (Esrafili-Dizaji and Rahimpour-Bonab 2009; Table 4), also compare closely with many of the values reconstructed using the medium-sized subset training images. On balance, this suggests that the training images that retain a higher resolution (medium-sized subsets) are most likely to more accurately reflect pore network architecture and subsequently permeability within this oolite.

Permeability values modeled for the Cretaceous laminite agree with data recorded by more traditional methods from other Brazilian laminites, with Miranda et al. (2016) measuring permeability of 0.00 to 0.09 mD (average 0.04 mD) and associated porosities of 4 to 22%

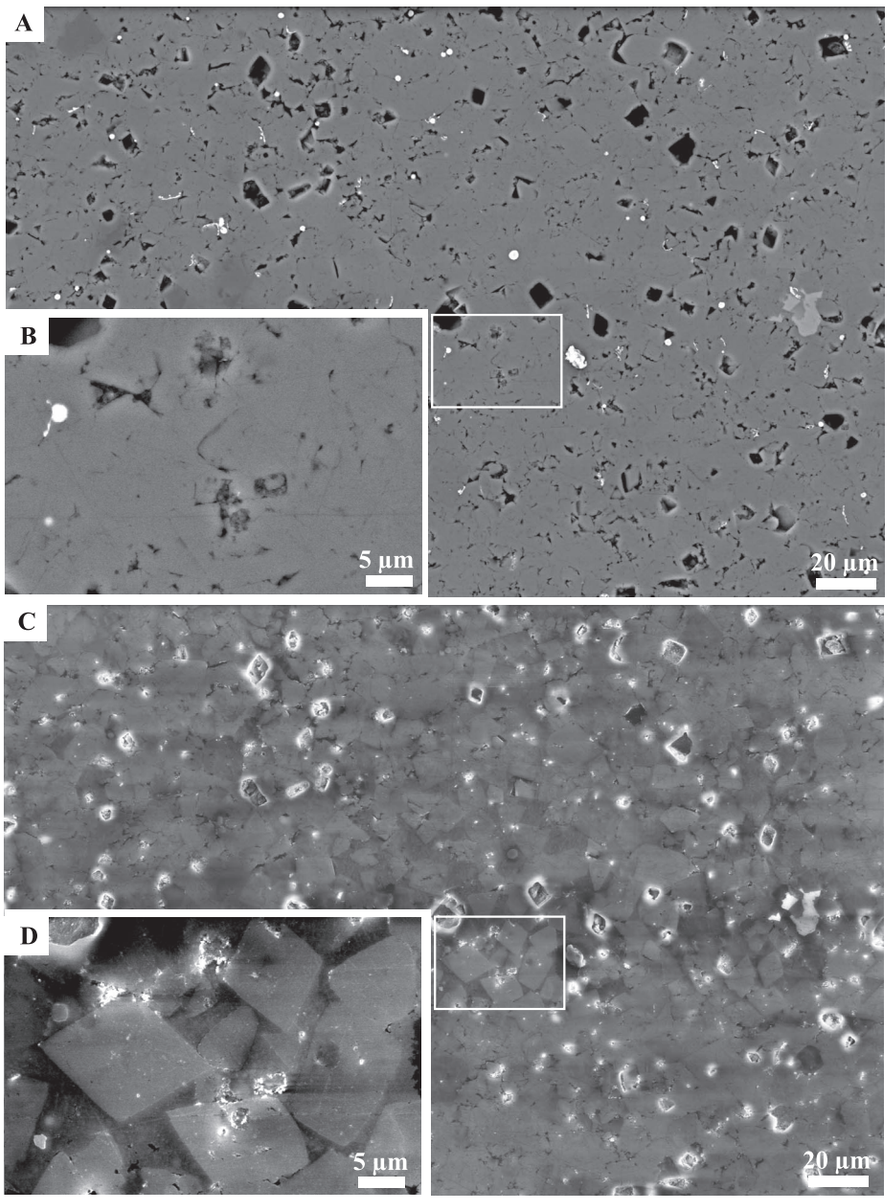

FIG. 12.—SEM montages of laminite. **A)** BSE montage, illustrating the occurrence of porosity (black), with details illustrated in inset **B)** from area marked by white box. **C)** Same area as in (A), with GSE detector montage, using the CCI technique. Note porosity is not as clearly displayed, but rhombic crystals are clearly displayed in inset image **D)** that are not seen in the BSE image (B).

(average 12%). These permeability values are all recorded across laminae, and they agree with equivalent measurements predicted from the larger laminite model (Table 3). High modeled values for permeability and flow parallel to micron- to millimeter-scale laminae (26.10 mD; Table 3) are harder to corroborate. Horizontal permeability values of 0.00 mD for low-porosity laminae (LaminiteC and LaminiteD models) are consistent with overall whole-rock values (see Miranda et al. 2016). However, the average permeability values for the more porous laminae (LaminiteA and LaminiteB) show a considerable difference when compared to permeability predicted for flow parallel to laminae from the larger-scale laminite model (Table 3). Of these, the lower values (average 1.43 and 2.70 mD) calculated for individual porous laminae are likely to be more representative. Higher values predicted for permeability parallel to porous laminae from the larger training image are likely to have been overestimated due to resolution issues connecting otherwise partially to poorly connected micropores. This is similar to the situation when modeling the oolite, and it indicates the importance of selecting representative areas for training images and the importance of image resolution.

The complexity and heterogenous nature of porosity within many carbonates make stochastic modeling, as illustrated here, particularly difficult. The relationships observed are often radically different to

Table 4.—Porosity and permeability data for oolites.

Porosity (%)	Permeability (mD)	Method	Source	Reference
36.1	494.61	Jorgensen equation	Savonnieres limestone	Moh'd (2009)
34.7	473.01			
30.6	177.42			
25 ± 0.3	29 ± 5	Gas perm	Savonnieres limestone	Lebedev et al. (2017)
18.6	—	XRT (dry)		
20.3	6.75	XRT (live brine)		
30–40	—	—	Savonnieres limestone	Fronteau et al. (2010)
25	1.5 to 2000	—	General	Zinszner and Pellerin (2007)
15.88	81.61	—	Permo–Triassic	Esrafili-Dizaji and Rahimpour-Bonab (2009)
21.98	50.12	—	Persian Gulf	
17.73	—	Nitrogen gas	Bicqueley Quarry	This paper
12.92	—			
11.87	—			

those observed in sandstones, upon which digital rock modeling (DRM) software is traditionally developed. In particular, with carbonates such as oolites, porosity can often be reversed from that at original deposition (Byrnes et al. 2003). Although not necessarily perfect, workable representations of pore networks for carbonates with unusual morphologies (oolite), or strong heterogeneities at the micron to millimeter scale (laminite) can be constructed that approach the structural complexity of the real world, and that provide better understanding of porosity and permeability variability. Permeability values generated from models for intraparticle microporosity within ooids are likely to be more realistic, but they do not reflect true permeability due to the lack of connectivity between ooids (cf. Byrnes et al. 2003, Zinszner and Pellerin 2007). Such pore spaces may have relevance where individual particles are connected (through compaction) or become connected through natural or artificial fracturing or acidification. As such, the permeability of apparently unconnected intraparticle microporosity or macromoldic porosity is still worth modeling, because it is difficult to measure directly. Such materials do, however, require careful consideration of scanned resolution used and the effective representative area selected. Nevertheless, results confirm the utility of the technique for producing reusable digital rock proxies for rock physics modeling.

Potential for Generating Multiple Porosity and Permeability Stochastic Models: Individual BSE tiles, or montaged sets of tiles, can be binarized for porosity and using stochastic 3D modeling to extract a range of porosity-permeability parameters. This can permit the calculation of permeability changes at the millimeter scale, which is over smaller areas than for traditional readings recorded from core. Currently, no automated options exist to transfer binarized images from SEM or image analysis into the stochastic pore network modeling workflow; this requires manual data input and output for each model constructed. Further developments in facilitating an interface to automate this procedure would more quickly characterize variability in permeability across geological carbonate materials (and others) at the micron to centimeter scale. Such data could then be transferred to packages such as Matlab for further analysis. In this fashion, it may become possible to model many thousands of permeability results (at the sub-millimeter to centimeter scale), and to plot these in a fashion similar to that used herein for contoured porosity data. Without automation for analysis of all collected images, selected areas of differing fabrics could be modeled separately and combined through stacking or model amalgamation to more fully define and reconstruct complex pore networks within carbonates, improving permeability predictions for heterogeneous carbonate systems at the micron to millimeter or even the centimeter scale.

GSE Montages and Tiles

In the case of the oolite, it is possible to document changes in cementation and final porosity, as well as details on the recrystallization and development of micritic fabrics. The latter is of great significance, because micrite has traditionally been viewed as simple mud, whereas the CCI technique offers a potential means by which to elucidate the paragenesis of micrites in general (e.g., within chalks). In the case of the laminite, CCI highlights the occurrence of rhombohedral calcite crystals, 5 to 20 μm in size, within a massive sparry calcite matrix, confirming the fine muddy micritic nature of these laminated lake carbonate sediments (cf. Catto et al. 2016, Miranda et al. 2016). There are, however, a number of areas that can require additional consideration when using the CCI technique to construct montages from large areas:

Improving CCI Contrast: CCI quality in terms of contrast, is generally highest at faster scan rates (3–5 μs), with slower scan rates (10–20 μs) resulting in decreasing contrast. This is somewhat problematic, because the best quality for BSE imaging typically requires a minimum scan rate of 10 μs. Since BSE and CCI images are obtained simultaneously (using the same scan rate), this means that automatically collected CCI images can lack good contrast. Contrast can be enhanced by increasing bias, although this typically introduces vertical bar artifacts (see below). However, image quality can be greatly improved (in terms of sharpness and contrast) through the integration of images obtained at fast scan rates. Although this is suitable for the collection of single images, the added acquisition load for large montages may not be practical. Some improvement in sharpness and contrast can be made in montages by selecting only two to three image scans per individual tile. The latter increases energy input, sharpness, and contrast without the drawbacks of slower scan speeds or higher bias values, and it is not too time-consuming. Where deemed necessary, montaged CCI images can be collected as per normal methods, and areas identified to be of significant interest can be scanned later as single images or as montages using frame integration at faster scan speeds.

CCI Montage Artifacts: CCI montages constructed across large areas of polished thin sections often exhibit strong changes in brightness (Fig. 13). These may be reduced by securing the margins of the thin section with conductive copper tape. Where the effect is

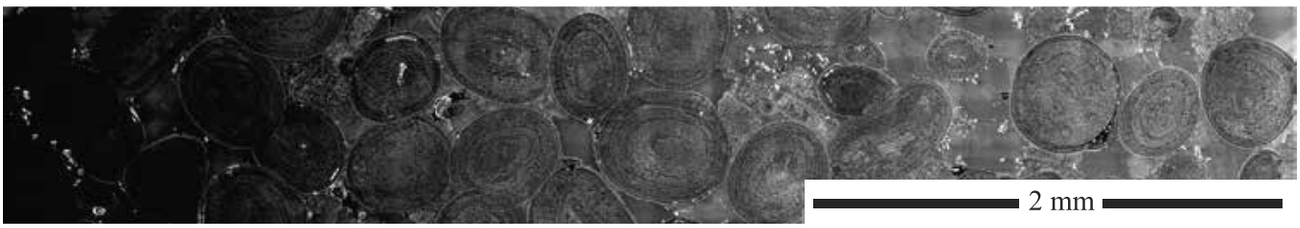

FIG. 13.—Example of GSE montage (comprising multiple tiles) exhibiting artifact typical of CCI montages, with large-scale progressive change in brightness across the montage caused by variability in electrical dissipation relative to position on the polished slide. Note: Small-scale vertical bar artifacts (see Fig. 14A) do not occur, as montage consists of tiles with 50% overlap.

particularly strong, however, it may be necessary to quickly scan the whole slide at lower resolution to determine stable areas of consistent contrast and brightness, which can then be scanned at higher resolution.

In addition, attempts to create a montage using the CCI technique commonly result in a patchwork appearance or the presence of unsightly broad vertical bands (Fig. 14A). These are the result of subtle changes in contrast due to consistent variation in surface charge (from left to right) across each individual tile, independent of tile position on the thin section. These variations are not particularly obvious within single images, but they are all too evident when tiles are stitched together. Such banding visually detracts from montages

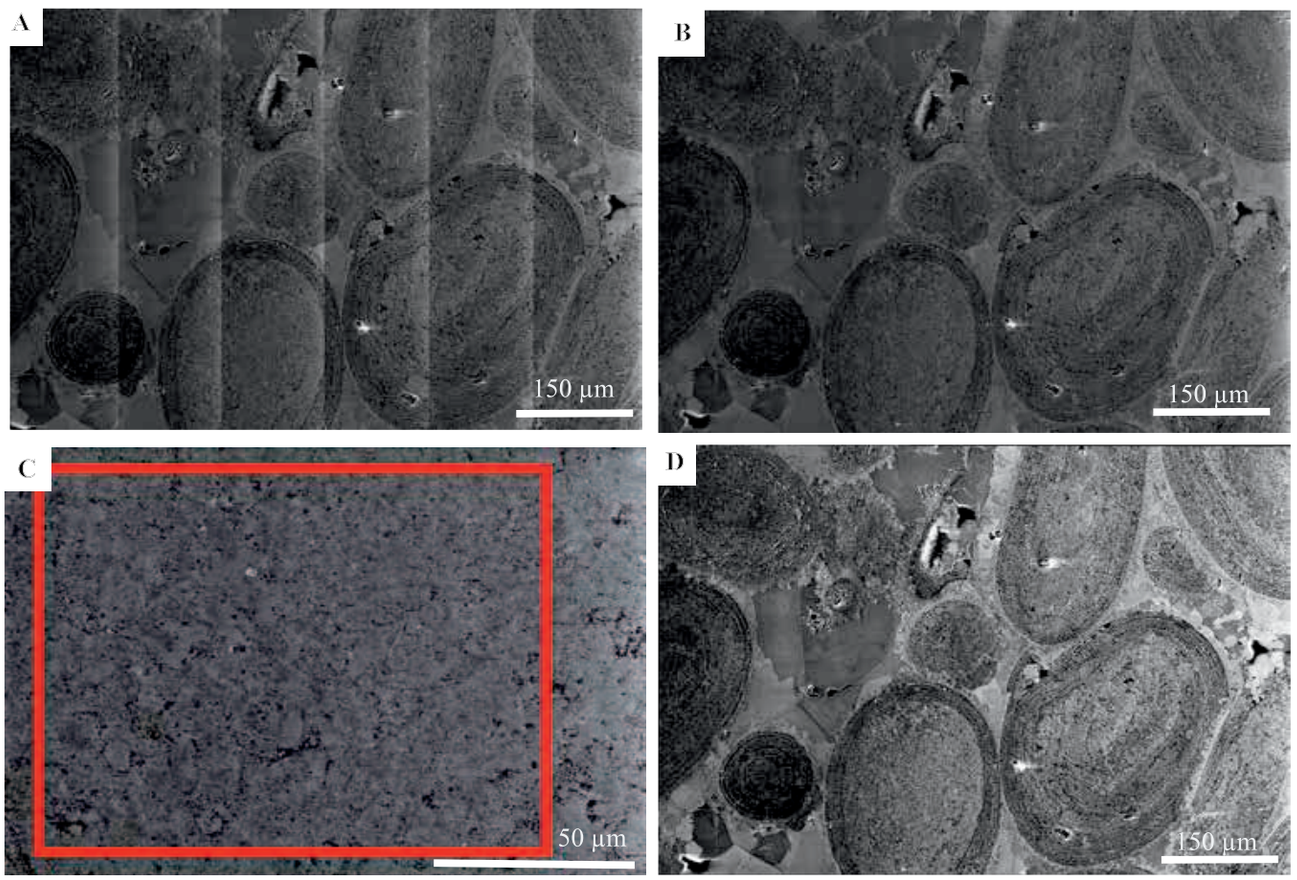

FIG. 14.—CCI of oolitic limestone, using GSE detector. **A)** Montaged image of a selected area, as in Fig. 10A. Individual tiles with 10% overlap, showing vertical banding. **B)** Same area as in (A) but with 50% overlap, exhibiting normal contrast across the montage. **C)** Single tile, from montage with 25% overlap of tiles, showing area to be cropped (red box). **D)** Montage of same area as in (A) and (B), with tiles acquired with 25% overlap, cropped as in (C), and stitched using Fiji software. Also see supplementary data for larger areas showing the difference between using 25% and 50% overlap.

and impedes their use in any form of image analysis. For individual images, contrast within CCI is maximized by increasing bias. However, higher bias values have the effect of increasing contrast artifacts along the left-hand margin of individual images, and therefore enhancing unwanted vertical banding within stitched montages. These can be reduced by limiting bias to between 40 and 50%, and two further methods can be employed to reduce such artifacts. The simplest method involves increasing tile overlap to 50% (Fig. 14B; supplementary Fig. S1), although this has a high cost in terms of additional time required to collect a montage. The second method involves collecting tiles with a 25% overlap (see supplementary Fig. S2), batch processing the tiles (e.g., using Fiji-ImageJ) to crop away the most affected marginal areas of the image (Fig. 14C), and stitching tiles together (Fig. 14D). The latter method is less costly in terms of acquisition times, but it may be neither efficient nor practical where montages consist of hundreds or thousands of tiles.

CONCLUSION

The automated collection of large-area, high-resolution montages from polished thin sections using SEM offers excellent opportunities for the study of depositional and diagenetic components within carbonates. BSE images can be employed directly in the study of pores, whereas GSE images utilizing the CCI technique can provide additional information on changes to porosity through time due to diagenesis as manifested by cementation and dissolution. CCI can be applied across a range of scales, providing information on the paragenesis of both sparry cements and micrite. Automated large-area high-resolution imaging by SEM offers a flexible visual approach that can be used to construct contoured plots on the variability of porosity in two dimensions, to display quantitative changes in porosity at the micron to millimeter scale, to plot linear changes in porosity in a manner similar to borehole logs, and through stochastic modeling to construct three-dimensional porosity networks, which can be later used to predict permeability. It is therefore possible to generate large-scale quantitative data on both porosity and permeability; at the same time, information on changes to original porosity and depositional fabrics brought about through paragenesis (cementation, recrystallization, and dissolution) can be qualitatively extracted. This combination of data has important applications for oil and gas reservoir development and production activities (e.g., Enhanced Oil Recovery), carbon sequestration, and reservoir stimulation (e.g., hydraulic fracturing).

SUPPLEMENTARY MATERIAL

The following supplementary material is available at the SEPM (Society for Sedimentary Geology) Book Supplemental Data site (www.sepm.org/Downloads.aspx).

Supplementary Figure S1. GSE montage of a selected area of oolitic limestone, with 50% overlap, displaying no artifacts.

Supplementary Figure S2. GSE montage of a selected area of oolitic limestone (as in Fig. S1), with 25% overlap, displaying vertical bar artifacts.

ACKNOWLEDGMENTS

The Center for Environmental Scanning Electron Microscopy (CESEM), Institute of Petroleum Engineering, Heriot-Watt University, is acknowledged for use of the facilities, without which this paper could not have been written. Many thanks go to the two reviewers (Chafetz and Hasiuk), associate editor (Gene Rankey) and editor (Don McNeil) for many helpful comments on the manuscript.

REFERENCES

Anovitz LM, Cole DR. 2015. Characterization and analysis of porosity and porestructures. *Reviews in Mineralogy and Geochemistry* 80:61–164.

Archie GE. 1952. Classification of carbonate reservoir rocks and petrophysical considerations. *American Association of Petroleum Geologists Bulletin* 36:278–298.

Berrezueta E, Gonzalez-Menendez L, Ordonez-Casado B, Olaya P. 2015. Pore network quantification of sandstones under experimental CO2 injection using image analysis. *Computers & Geosciences* 77:97–110.

Buckman JO. 2014. Use of automated image acquisition and stitching in scanning electron microscopy: Imaging of large scale areas of materials at high resolution. *Microscopy and Analysis (Europe)* 28:S13–S15.

Buckman JO, Bankole SA, Zihms S, Lewis H, Couples G, Corbett PWM. 2017. Quantifying porosity through automated image collection and batch image processing: Case study of three carbonates and an aragonite cemented sandstone. *Geosciences* 7(3):70. DOI:10.3390/geosciences7030070

Buckman JO, Corbett PWM, Mitchell L. 2016. Charge contrast imaging (CCI): Revealing enhanced diagenetic features of a coquina limestone. *Journal of Sedimentary Research* 86:734–748.

Byrnes AP, Franseen EK, Watney WL, Dubois MK. 2003. The Role of Moldic Porosity in Paleozoic Kansas Reservoirs and the Association of Original Depositional Facies and Early Diagenesis with Reservoir Properties: Kansas Geological Survey. Open-File Report 2003-32. http://www.kgs.ku.edu/PRS/publication/2003/ofr2003-32/P1-02.html. Accessed October 2, 2018.

Catto B, Jahnert RJ, Warren LV, Varejao FG, Assine ML. 2016. The microbial nature of laminated limestones: Lessons from the Upper Aptian, Araripe Basin, Brazil. *Sedimentary Geology* 341:304–315.

Chen L, Zhang L, Kang Q, Viswanathan HS, Yao J, Tao W. 2015. Nanoscale simulation of shale transport properties using the lattice Boltzmann method: Permeability and diffusivity. *Nature Scientific Reports* 5:8089. DOI:10.1038/srep08089

Choquette PW, Pray LC. 1970. Geologic nomenclature and classification of porosity in sedimentary carbonates. *American Association of Petroleum Geologists Bulletin* 54:207–250.

Cuthbert SJ, Buckman JO. 2005. Charge contrast imaging of fine-scale microstructure and compositional variation in garnet using the environmental scanning electron microscope. *American Mineralogist* 90:701–707.

Doehne E, Carson D. 2001. Charge contrast imaging (CCI) in the environmental scanning electron microscope: Optimizing operating parametres for calcite. *Microscopy and Analysis (New York)* 7:780–781.

Esrafili-Dizaji B, Rahimpour-Bonab H. 2009. Effects of depositional and diagenetic characteristics on carbonate reservoir quality: A case study from the South Pars gas field in the Persian Gulf. *Petroleum Geoscience* 15:325–344.

Fronteau G, Scheider-Thomachot C, Chopin E, Barbin V, Mouze DM, Pascal A. 2010. Black-crust growth and interaction with underlying limestone microfacies. *In* Prikryl R, Török A (Editors). *Natural Stone Resources for Historical Monuments*, Special Publication 333: Geological Society, London. p. 25–34.

Griffin BJ. 1997. A new mechanism for the imaging of crystal structure in non-conductive materials: An application of charge-induced contrast in the environmental scanning electron microscope (ESEM). *Microscopy and Microanalysis* 3:1197–1198.

Griffin BJ. 2000. Charge contrast imaging of material growth and defects in ESEM—Linking electron emission and cathodoluminescence. *Scanning* 22:234.

Hollis C, Vahrenkamp V, Tull S, Mookerjee A, Taberner C, Huang Y. 2010. Pore system characterization in heterogeneous carbonates: An alternative approach to widely-used rock-typing methodologies. *Marine and Petroleum Geology* 27:772–793.

Hosa A, Curtis A, Wood R. 2016. Calibrating lattice Boltzmann flow simulations and estimating uncertainty in the permeability of complex porous media. *Advances in Water Resources* 94:60–74.

Huang T, Jiang Z, van Dijke R, Geiger S, Petrovskyy D. 2018. Reconstruction of complex 3D pore structure in carbonates from 2D images using global optimization. Interpore 2018, New Orleans, Louisiana 14–17 May 2018.

https://events.interpore.org/event/2/contributions/815/. Accessed October 2, 2018.

Jiang Z, van Dijke MIJ, Wu K, Couples GD, Sorbie KS, Ma J. 2012. Stochastic pore network generation from 3D rock images. *Transport in Porous Media* 94:571–593.

Jiang Z, Wu K, Couples G, van Dijke M, Sorbie KS, Ma J. 2007. Efficient extraction of pore networks from three-dimensional porous media. *Water Resources Research* 43:2578–2584.

Lebedev M, Zhang Y, Sarmadivaleh M, Barifcani A, Al-Khdheeawi E, Iglauer S. 2017. Carbon geosequestration in limestone: Pore-scale dissolution and geomechanical weakening. *International Journal of Greenhouse Gas Control* 66:106–119.

Lemmens H, Richards D. 2013. Multiscale imaging of shale samples in the scanning electron microscope. *In* Camp W, Diaz E, Wawak B (Editors). *Electron Microscopy of Shale Hydrocarbon Reservoirs*, Memoir 102: American Association of Petroleum Geologists, Tulsa, Oklahoma. p. 27–35.

Lucia FJ. 1995. Rock-fabric/petrophysical classification of carbonate pore space for reservoir characterization. *American Association of Petroleum Geologists Bulletin* 79:1275–1300.

Marzouk I, Takezaki H, Miwa M. 1995. Geologic controls on wettability of carbonate reservoirs, Abu Dhabi, U.A.E., 11–14 March 1995, SPE-29883. Middle East Oil Show. Society Petroleum Engineering, https://www.onepetro.org/conference-paper/SPE-29883-MS. Accessed October 2, 2018.

Marzouk I, Takezaki H, Susuki M. 1998. New classification of carbonate rocks for reservoir characterization, Abu Dhabi, UAE, 7–10 November 1998, SPE-49475. 8th Abu Dhabi International Petroleum Exhibition and Conference. Society Petroleum Engineering, https://www.onepetro.org/conference-paper/SPE-49475-MS. Accessed October 2, 2018.

Mazurkiewicz L, Mlynarczuk M. 2013. Determining rock pore space using image processing methods. *Geology, Geophysics & Environment* 39:45–54.

Miranda T, Barbosa A, Gomes I, Soares A, Santos R, Matos G, McKinnon E, Neumann V, Marrett R. 2016. Petrophysics and petrography of Aptian tight carbonate reservoir, Araripe Basin, NE Brazil 78th EAGE Conference & Exhibition 2016; Vienna, Austria; May 30–June 2, 2016. http://www.earthdoc.org/publication/publicationdetails/?publication=85135. Accessed October 2, 2018.

Moh'd BK. 2009. Compressive strength of vuggy oolitic limestones as a function of their porosity and sound propagation. *Jordan Journal of Earth and Environmental Sciences* 2:18–25.

Ott H, Pentland CH, Oedal S. 2015. CO_2-brine displacement in heterogeneous carbonates. *International Journal of Greenhouse Gas Control* 33:135–144.

Pak T, Butler I, Geiger S, Van Dijke MIJ, Jiang Z, Surmas R. 2016. Multiscale pore-network representation of heterogeneous carbonate rock. *Water Resource Research* 52:5433–5441.

Prammer MG, Drack ED, Boulton JC, Gardner JS, Coates GR, Chandler RN, Miller MN. 1996. Measurements of clay-bound water and total porosity by magnetic resonance logging, SPE-36522-Ms. SPE Annual Technical Conference and Exhibition; Denver, Colorado; October 6–9, 1996. Society of Petroleum Engineering p. 311–321. https://www.onepetro.org/conference-paper/SPE-36522-MS. Accessed October 2, 2018.

Ramamoorthy R, Boyd A, Neville TJ, Seleznev N, Sun H, Flaum C, Ma J. 2010. A new workflow for petrophysical and textural evaluation of carbonate reservoirs. *Petrophysics* 51:17–31.

Rios EH, Moss AK, Pritchard TN, Domingues ABG, de Vasconcellos Azeredo RB. 2015. Carbonate NMR permeability estimates based on the Winland-Pittman MICP approach. *In* International Symposium of the Society of Core Analysts; St. John's Newfoundland and Labrador, Canada; August 16–21, 2015. SCA2015-037. https://pdfs.semanticscholar.org/4af9/dc0b0c632fa94950e0590b7cbc0909b6d1de.pdf. Accessed October 2, 2018.

Ryazanov A, van Dijke M, Sorbie M. 2009. Two-phase pore-network modelling: Existence of oil layers during water invasion. *Transport in Porous Media* 80:79–99.

Van Dijke MIJ, Jiang Z, Wu K, Wang C, Al-Abri M, Sorbie K, Couples G. 2011, Prediction of multi-phase flow properties of heterogeneous rocks based on stochastic pore-network generation. International Conference on Flows and Mechanics in Natural Porous Media from Pore to Field Scale—Pore2Field; Paris; November, 16–18, 2011. IFP Energies Nouvelles/Rueil-Malmaison, Paris, November 2011. https://www.researchgate.net/publication/266885779_Prediction_of_multi-phase_flow_properties_of_heterogeneous_rocks_based_on_stochastic_pore-network_generation. Accessed October 2, 2018.

Watt GR, Griffin BJ, Kinny PD. 2000. Charge contrast imaging of geological materials in the environmental scanning electron microscope. *American Mineralogist* 85:1784–1794.

Wu K, Van Dijke MIJ, Couples GD, Jiang Z, Ma J, Sorbie KS, Crawford J, Young I, Zhang X. 2006. 3D stochastic modelling of heterogeneous porous media—Applications to reservoir rocks. *Transport in Porous Media* 65:443–467.

Zinszner B, Pellerin FM. 2007. *A Geoscientist's Guide to Petrophysics*: IFP Publications, Editions TECHNIP, Paris. 384 p.